

## Facile dual-shot measurement of Schmidt number in type-0 and type-2 downconversion

Vikas S. Bhat , Kiran Bajar , Rounak Chatterjee, and Sushil Mujumdar <sup>\*</sup>  
*Tata Institute of Fundamental Research, 400005 Mumbai, India*

 (Received 17 May 2024; accepted 18 July 2024; published 8 August 2024)

High-dimensional entangled states have now been identified as excellent candidates towards the enhancement of the bandwidth of quantum systems. A variety of methods exist that aim to certify and set the bounds to entanglement. However, rapid and accurate approaches for precise quantification of the dimensions remain a challenge. Here, we report a facile, rapid and robust approach that quantifies a wide range of the spatial dimensions of high-dimensional entangled states using an interferometric technique using only two images. Our process works for a class of pure two-photon states, regardless of its separability and provides a fast and easy way to accurately measure the spatial Schmidt number which is a quantitative measure of dimensionality of entanglement. We apply our method to two-photon states generated by spontaneous parametric down-conversion (SPDC) and show that our results are in excellent agreement with numerical estimates. Since such estimates only exist for collinear phase matching in SPDC crystals, we also derive a noncollinear phase-matching condition applicable for type-2 crystals. In these nonlinear crystals, the commonly applied assumption of degenerate daughter photons no longer holds, leading to deviations from earlier theoretical predictions. Our interferometric technique provides excellent results for both type-0 and type-2 collinear phase-matching conditions, endorsing its wide applicability in quantum photonics.

DOI: [10.1103/PhysRevResearch.6.033151](https://doi.org/10.1103/PhysRevResearch.6.033151)

### I. INTRODUCTION

From its inception till today, entanglement remains one of the most curious aspects of quantum mechanics. It was first pointed out by Einstein, Podolsky, and Rosen (EPR) [1] and Schrödinger [2] by showing that some multiparticle quantum states have global states without meaningful composite states. Bohm [3] reformulated the EPR argument in terms of a simpler bipartite system of two spin-1/2s using which Bell proposed his famous inequality [4]. Experimental violations of this inequality distinguish the predictions of quantum mechanics and a theory based on local hidden variables. These experiments [5–8] ruled in the favour of quantum mechanics. It is curious to note that, while these experiments were based on two-dimensional Hilbert space (qubits), the EPR work dealt with continuous variable entanglement, that is, high dimensional entanglement. These states were not studied extensively owing to their complexity. Work on high-dimensional entanglement picked up momentum with Werner's contribution [9] where the first formal definition of entanglement was provided.

Recently, however, high-dimensional entangled states have grown popular as they can be readily used to in-

crease the bandwidth and security bounds for quantum communication by opening up higher dimensions of Hilbert space [10]. Several reports have catalogued the benefits of these high-dimensional spaces by using energy-time, angle-orbital angular momentum, and transverse momentum-spatial degrees of freedom [11,12]. Other reports have also shown how higher dimensions enable information processing that is robust against noise [13], and optimal quantum cloning machines [14,15]. They have been employed to enhance the information transfer rates [16], making them superior to the qubit alternatives for applications in quantum information and quantum communication. For a broader introduction to continuous variable entanglement, we refer to Ref. [17].

An existing challenge in high-dimensional systems is the absence of a reliable way to certify and quantify the entanglement, especially in the presence of noise [18,19]. It is known that, in case of high-dimensional entanglement, certification is comparatively easier than its quantification [20]. Analogous to the Bell's inequality whose violation certifies the presence of qubit entanglement, various inequalities exist for continuous variable-correlations. Many studies have measured EPR-correlations to certify position-momentum [21–28], angle-orbital angular momentum [29], radial position-radial momentum [30], quadrature phase-amplitude [31], and time-energy [32–34] entanglement. There are a few techniques to quantify the entanglement such as quantum state tomography [35–39], however, these techniques do not scale well with dimension. Moreover, methods based on mutually unbiased bases [36,37] only provide bounds. Next, a few established coincidence-based measurements exist in the field [40–42] that are reported to scale well, but they incur long experimental duration and loss of

<sup>\*</sup>Contact author: [mujumdar@tifr.res.in](mailto:mujumdar@tifr.res.in);  
<http://www.tifr.res.in/~nomol>

*Published by the American Physical Society under the terms of the Creative Commons Attribution 4.0 International license. Further distribution of this work must maintain attribution to the author(s) and the published article's title, journal citation, and DOI.*

partner photons, which adversely affect their accuracy. They also require prior knowledge of the form of the underlying state. Part of the long runtime in some methods arises from the raster scanning of single-photon detectors, a process that can be circumvented by innovative two-dimensional quantum detection [43–45]. Nonetheless, it is crucial to measure, in a rapid and facile manner, the dimensions of these states for fundamental tests of quantum mechanics as well as for practical applications of quantum information processing protocols and quantum communication systems. In the former, the dimension sets the bounds for inequality while in the latter two, dimensions set the information capacity of the state as well as the security bounds of the communication channel.

It is now known that measurements based on intensity detection can provide superior accuracy compared to those based on coincidence detection. The dimensionality of entanglement is quantified by a parameter called the Schmidt number [46], defined as the minimum number of independent vectors obtained by the Schmidt decomposition of the density matrix. The Schmidt decomposition in quantum theory is deeply connected to the coherent-mode decomposition in classical coherence theory [47]. This connection was exploited to experimentally demonstrate [47] that, for a pure state, the two-photon spatial Schmidt number can be measured by implementing intensity measurements on only one of the photons. However, this technique only works in the highly entangled state, whose reduced state behaves as a quasi-homogeneous source. Later, in the context of entanglement migration [41], it was shown [42] that the dimensionality of spatial entanglement is inversely proportional to the interference visibility of one of the photons. However, they eventually measured the Schmidt number by a coincidence method because the visibility of the one-photon interference is very sensitive to noise and always overestimates the dimensions. In this work, we establish an inversion-interferometric technique (interference between a source and its inversion) to measure the spatial Schmidt number with just two images that is robust to noise. Such inversion interferometers were proposed in Ref. [41] and were later deployed [42,48,49] to measure various quantities such as EPR-correlations and orbital angular momentum spectra. In this work, using theoretical considerations, we find that the inversion interferometer has further information encoded in it. Accordingly, we report a way to extract the spatial Schmidt number based on intensity measurements for two-photon states that are pure, irrespective of whether the state is separable or entangled. This also includes slightly entangled states as long as certain conditions, as stated later, are met.

The rest of the paper is divided into two sections and three appendices. Section II sets up the theoretical background of higher dimensional entanglement in the context of transverse momentum and how Schmidt number encapsulates its measure. In Sec. II A, we examine the form of the wave function used in typical SPDC experiments and derive the Schmidt number for it, while in Sec. II B, we also show why it is inapplicable for certain wave functions. In Sec. III A, we elaborate our experimental setup and in Sec. III B, we present the results.

## II. THEORY

In the transverse momentum basis, a general two-photon pure state  $|\psi\rangle$  can be expressed as

$$|\psi\rangle = \iint d\mathbf{q}_1 d\mathbf{q}_2 \psi(\mathbf{q}_1, \mathbf{q}_2) |\mathbf{q}_1, \mathbf{q}_2\rangle, \quad (1)$$

where  $\mathbf{q}_1 = (k_{1x}, k_{1y})$  and  $\mathbf{q}_2 = (k_{2x}, k_{2y})$  are the transverse wave vectors of the daughter photons,  $|\mathbf{q}_1, \mathbf{q}_2\rangle$  is the two-photon momentum state and  $\psi(\mathbf{q}_1, \mathbf{q}_2)$  is the two-photon wave function. If this wave function can be written as  $\psi(\mathbf{q}_1, \mathbf{q}_2) = u(\mathbf{q}_1)v(\mathbf{q}_2)$ , it is separable. If such a separation does not exist, the state is said to be entangled.

A natural way to characterize the structure of entanglement of a pure state is via a Schmidt decomposition. For the wave function in Eq. (1), it is given by

$$\psi(\mathbf{q}_1, \mathbf{q}_2) = \sum_{n=0}^{\infty} \sqrt{\beta_n} u_n(\mathbf{q}_1) v_n(\mathbf{q}_2). \quad (2)$$

Here  $u_n(\mathbf{q}_1)$  and  $v_n(\mathbf{q}_2)$  are the Schmidt modes. These are the eigenmodes of the reduced density matrices of the signal (first photon) and idler (second photon) respectively with  $\beta_n$  being the corresponding eigenvalues. Since the trace of the (reduced) density matrix is equal to the sum of its eigenvalues, we have  $\sum_n \beta_n = 1$ .

Even though our state lies in an infinite dimensional Hilbert space of continuous parameters, the finiteness of the trace of density matrix ensures that the Schmidt decomposition is always discrete [50]. Such a decomposition naturally partitions itself to reveal how the photons are paired since if signal is detected in mode  $u_n$  it immediately implies that the idler is in the mode  $v_n$ . Furthermore, the eigenvalues  $\beta_n$  provide a measure of the degree of entanglement as they provide a weight factor to each mode. If there was only mode  $n = 1$ , the trace condition gives us  $\beta_1 = 1$  and that state is hence separable. In the maximally entangled case in  $N$  dimensions, we have  $\beta_n = 1/N$ . The Schmidt number  $K$  defined as  $K \equiv 1/\sum_n \beta_n^2$  provides an ‘‘average’’ measure of the number of Schmidt modes involved in the decomposition of Eq. (2). Unlike the eigenvalues  $\beta_n$ s, the Schmidt number  $K$  is directly measurable in experiments and thus is a more direct measure of entanglement.

### A. The SPDC wave function and its Schmidt number

A common way to generate such high-dimensional entangled states is via a nonlinear optical process called spontaneous parametric down-conversion (SPDC). Here, one pump photon is down-converted to two lower-frequency photons, named signal and idler. Since the process is parametric, it conserves energy, momentum and angular momentum which is the source of entanglement between the daughter photons. The conservation of energy and momentum imply that,

$$\omega_p = \omega_1 + \omega_2, \quad \mathbf{k}_p = \mathbf{k}_1 + \mathbf{k}_2,$$

where  $\omega_p$  is the frequency,  $\mathbf{k}_p$  is the wave vector of the pump photon and  $\omega_i$  is the frequency and  $\mathbf{k}_i$  is the wave vector of the

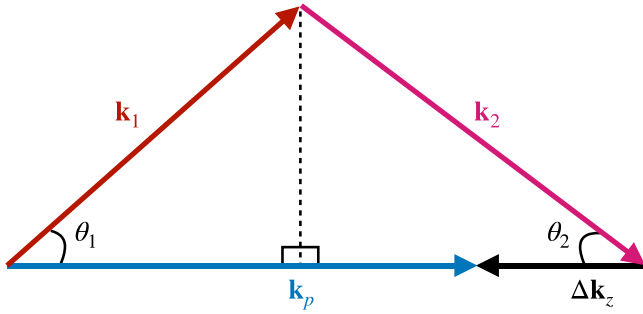


FIG. 1. Momentum conservation between the pump (blue line) and the nondegenerate daughter (red and magenta lines) photons.

daughter photon(s) with  $i = 1, 2$ . For the degenerate case, the componentwise momentum relation (see Fig. 1) is given by

$$k_p = (k_1 + k_2) \cos(\theta) - \Delta k_z, \quad (3)$$

$$\frac{|q_1 - q_2|}{2} = k_1 \sin(\theta), \quad (4)$$

where  $\theta$  is the angle between pump momentum  $k_p$  and the signal or idler (degenerate) momentum vectors  $k_1$  and  $k_2$ . Under the paraxial approximation, that is for small angle  $\theta$ , we can combine Eqs. (3) and (4) to get

$$\Delta k_z \approx -\frac{|q_1 - q_2|^2}{2k_p}. \quad (5)$$

We simplify the form of SPDC wave function under the following five assumptions.

(i) The pump is monochromatic whose longitudinal momentum is much greater than the transverse components. This assumption is approximately achieved experimentally by using narrowband laser and proper collimation.

(ii) The pump is sufficiently bright so that the downconversion events negligibly affect its intensity. Conventional pump lasers and crystal efficiencies are well-aligned with this assumption.

(iii) The downconversion is perfectly energy conserving ( $\Delta\omega = 0$ ) and the daughter photons are degenerate ( $\omega_1 = \omega_2$ ). This is achieved experimentally by using appropriate nonlinear crystals, augmented by narrowband filters for the downconverted beam.

(iv) The pump wavelength is much smaller than the transverse dimensions of the crystal, which is easily achieved in conventional crystals.

(v) The daughter photons are in the paraxial regime, which can be ensured using proper pump beam characteristics.

These conditions, particularly the last two, mean that the downconverted wave function can be partitioned into  $\psi(\mathbf{q}_1, \mathbf{q}_2) = \psi(\mathbf{q}_1 + \mathbf{q}_2)\psi(\mathbf{q}_1 - \mathbf{q}_2)$  [51]. The first term, with the summed momenta as the argument, arises from the largeness condition of the crystal, while the second term originates from the paraxial approximation.

Finally, following Ref. [51], a Gaussian pump beam with its waist at the crystal center yields the two-photon wave function in the momentum space that can be approximated as

$$\psi(\mathbf{q}_1, \mathbf{q}_2) = A e^{-|\mathbf{q}_1 + \mathbf{q}_2|^2/4\sigma_k^2} e^{-b^2|\mathbf{q}_1 - \mathbf{q}_2|^2/4}, \quad (6)$$

where  $A$  is the normalization constant,  $\sigma_k$  is the inverse of the pump beam waist  $w_0$  and  $b^2 = L/3k_p$ , where  $L$  is the crystal length and  $k_p$  is the pump wave number inside the crystal. Evidently, the two-photon wave function is a product of two Gaussians, one in the sum of transverse momenta and another in their difference. The advantage of this double-Gaussian (DG) approximation is that its statistical properties, the marginal, and conditional distributions are easy to compute. Furthermore, for this DG wave function, the Schmidt modes are the energy eigenfunctions of the 2D isotropic harmonic oscillator. The Schmidt number  $K$  is the inverse sum of squared probabilities of each eigenmode (by definition) and is given by [50]

$$K = \frac{1}{4} \left( b\sigma_k + \frac{1}{b\sigma_k} \right)^2. \quad (7)$$

It is to be noted that our  $b$  value differs from Ref. [50] as we use the momentum matching method introduced in Ref. [51]. This is appropriate as we are working in the momentum space. Thus, to measure  $K$  experimentally, we need to accurately measure the widths  $b$  and  $\sigma_k$  of our DG wave function.

For ease of calculation of the widths, we define rotated coordinates  $\mathbf{q}_\pm = (\mathbf{q}_1 \pm \mathbf{q}_2)/\sqrt{2}$ , with their variances under the transformed DG wave function labeled  $\sigma_\pm^2$ . The marginal  $\sigma_1$  and conditional  $\sigma_{(1|2)}$  for a DG can now be written as

$$\sigma_1^2 = \frac{\sigma_+^2 + \sigma_-^2}{2} \quad \sigma_{(1|2)}^2 = \frac{2\sigma_+^2\sigma_-^2}{\sigma_+^2 + \sigma_-^2}. \quad (8)$$

Furthermore, in terms of the rotated coordinates, the factor  $b\sigma_k = \sigma_+/\sigma_-$ . In terms of the rotated variances, the 2D Schmidt number, which due to azimuthal symmetry is the square of the 1D variant, is given by [51]

$$\begin{aligned} K &= \frac{1}{4} \left( \frac{\sigma_+}{\sigma_-} + \frac{\sigma_-}{\sigma_+} \right)^2 = \left( \frac{\sigma_+^2 + \sigma_-^2}{2\sigma_+\sigma_-} \right)^2 \\ &= \left( \frac{\sigma_+^2 + \sigma_-^2}{2} \right) \left( \frac{\sigma_+^2 + \sigma_-^2}{2\sigma_+^2\sigma_-^2} \right). \end{aligned} \quad (9)$$

Using Eq. (8) in Eq. (9),

$$K = \frac{\sigma_1^2}{\sigma_{(1|2)}^2}. \quad (10)$$

Thus, under the DG approximation for the wave function, the Schmidt number is just a ratio between the marginal and the conditional variance of the wave function, also known as the Fedorov ratio [52]. It is well-known that for a DG wave function, the Fedorov ratio and the Schmidt number become identical at the imaging and Fourier planes of the crystal center [42]. Thus, in order to measure the dimensions of our state, we can replace the tedious measurement of  $b$  and  $\sigma_k$  with the much simpler measurement of the conditional and marginal variances.

Recently, it was shown that the correlation width of a biphoton state  $\psi(\mathbf{q}_1, \mathbf{q}_2)$  can be extracted from inversion interferometry [49]. The cross term of an interference, given by the one-photon cross-spectral density function is

$$W(\mathbf{q}_1, \mathbf{q}'_1) = \iint \psi^*(\mathbf{q}_1, \mathbf{q}_2)\psi(\mathbf{q}'_1, \mathbf{q}_2)d\mathbf{q}_2.$$

Whenever  $\psi$  obeys

$$\psi^*(\mathbf{q}_1, \mathbf{q}_2)\psi(-\mathbf{q}_1, \mathbf{q}_2) \propto |\psi(\mathbf{q}_1, \mathbf{q}_2 = 0)\psi(\mathbf{q}_1 = 0, \mathbf{q}_2)|^2, \quad (11)$$

the conditional momentum probability distribution  $P(\mathbf{q}_1|\mathbf{q}_2 = 0)$  is related to the cross-spectral density as follows [49]:

$$W(\mathbf{q}_1, -\mathbf{q}_1) \propto P(\mathbf{q}_1|\mathbf{q}_2 = 0). \quad (12)$$

This implies that the conditional distribution has the same width as the cross-spectral density. To obtain the width  $\sigma_{(1|2)}$  of  $P(\mathbf{q}_1|\mathbf{q}_2 = 0)$ , we can measure the width  $f$  of  $W(\mathbf{q}_1, -\mathbf{q}_1)$ .

Thus we can finally rewrite Eq. (10) in our context as

$$K = \left(\frac{\sigma}{f}\right)^2 \quad (13)$$

since in our case the marginal distribution is the downconverted beam,  $\sigma$  is just the width of the beam (we have dropped the inconsequential index) and the width of the conditional as we saw in Eq. (12) is the (fringe) width  $f$  of the cross-spectral density. Although we derived the Schmidt number at the momentum plane, the ratio of widths in Eq. (10) is also the inverse visibility of the interferometer, as clarified in Appendix A. This implies that the ratio is equal to the Schmidt number at all locations and not just the momentum/position plane. Since our method relies on fringe width rather than fringe visibility, it is insensitive to noise, loss of partner photon, unequal polarization, or unequal intensities from the two arms of OEMZI making it robust. The error in the product of the position and momentum frame fringe widths of a mixed state when compared to a pure state has been shown to scale linearly with the fraction of mixedness of the state [49].

### B. Type-2 SPDC wave function

Our theory in the previous section makes the implicit assumption that the two downconverted photons are degenerate. This implies perfect phase matching for which the wave function is easy to compute. We now use the general momentum conservation to derive a more appropriate wave function. The momentum conservation componentwise, is given by

$$k_p = k_1 \cos \theta_1 + k_2 \cos \theta_2 + \Delta k_z + k_{pp}, \quad (14)$$

$$|\mathbf{q}_1 - \mathbf{q}_2| = k_1 \sin \theta_1 + k_2 \sin \theta_2, \quad (15)$$

where  $k_{pp} = 2\pi/\Lambda$  is the contribution coming from periodic poling with a period of  $\Lambda$ . Under the small angle approximation we can rewrite Eq. (14) in terms of the wavelengths  $\lambda_i$  as

$$\frac{\Delta k_z}{2\pi} = \left(\frac{n_p}{\lambda_p} - \frac{n_1}{\lambda_1} - \frac{n_2}{\lambda_2} - \frac{1}{\Lambda}\right) + \frac{n_1 \theta_1^2}{2\lambda_1} + \frac{n_2 \theta_2^2}{2\lambda_2},$$

where  $n_i$  are the refractive indices along the appropriate daughter photon's polarization vector. We note that the first term of the above equation is independent of the angle, i.e., the transverse momenta, while the subsequent part has two different angles as the daughter photons are no longer degenerate. The angle independent part is known as the collinear phase mismatch as it leads to noncollinear downconversion. The phase mismatch factor is non-negligible for a type-2 downconversion. Owing to its birefringence, the contribution

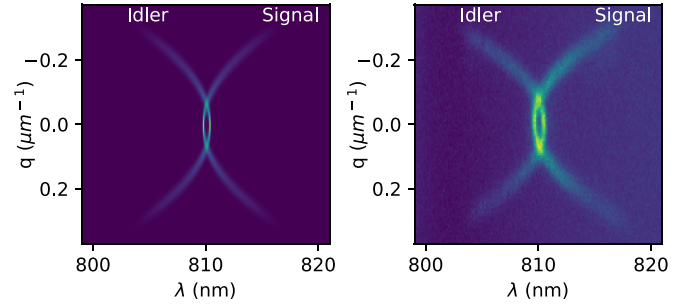


FIG. 2. Numerically calculated (left) and experimentally measured (right) type-2 wave function projected in the transverse  $y$  momentum and the spectral basis. The temperature of the crystal (length 30 mm) is set to  $40^\circ\text{C}$  to ensure maximum degeneracy. Each plot is made up of two curves, the positively curved ordinary signal and the negatively curved extraordinary idler. The horizontal spread in the experimental figure comes from nonzero bandwidth of the pump.

from unequal refractive indices experienced by the daughter photons leads to a broader bandwidth. Further comments on the structure of this wave function are given in Appendixes B and C.

Now using Eq. (15) under the small angle approximation, our above equation further simplifies to

$$\frac{\Delta k_z}{2\pi} = \left(\frac{n_p}{\lambda_p} - \frac{n_1}{\lambda_1} - \frac{n_2}{\lambda_2} - \frac{1}{\Lambda}\right) + \left(\frac{\lambda_1 + \lambda_2}{n_1 + n_2}\right) \frac{|\mathbf{q}_1 - \mathbf{q}_2|^2}{32\pi^2}. \quad (16)$$

Thus a more accurate SPDC wave function would be one where the argument of the second Gaussian in Eq. (6) is replaced with the right hand side of Eq. (16). The numerically simulated reduced type-2 wave function expressed in the transverse  $y$  momentum and wavelength basis is depicted in the left image of Fig. 2, while the corresponding experimental measurement is depicted on the right. We use a 10 nm bandwidth filter function corresponding to the filter used experimentally. Since the phase-mismatch is minimum at a crystal temperature of  $40^\circ\text{C}$ , the simulation and experiment are run at that temperature. The temperature-dependent refractive index as a function of wavelength is taken from [53].

The wave function is made of two curves (Fig. 2). The one on the left corresponds to the idler and the right one corresponds to signal. Since the system is azimuthally symmetric, we can rotate Fig. 2 about the  $q = 0$  axis to get the full momentum wave function in the cylindrical coordinates  $(\mathbf{q}, \lambda)$ . If the signal is found at a certain  $(\mathbf{q}, \lambda)$ , then the idler is found at  $(-\mathbf{q}, \lambda')$ . We note that the difference in the daughter photon's wavelengths  $|\lambda - \lambda'|$  increases with the transverse momentum  $\mathbf{q}$ . Thus, we find that, in the momentum space, the type-2 SPDC beam is not just made up of a single structure. It has a degenerate central disk surrounded by nondegenerate rings of various radii and this nondegeneracy increases radially. Such a structure of the wave function has been mentioned earlier in terms of a phase mismatch factor [54], but its wavelength dependence is hitherto unstudied.

Since the theory in Sec. II A only works for degenerate daughter photons, it is only applicable to the central section of the general wave function (see Fig. 2), we need to filter out the degenerate center either spectrally or spatially. The former

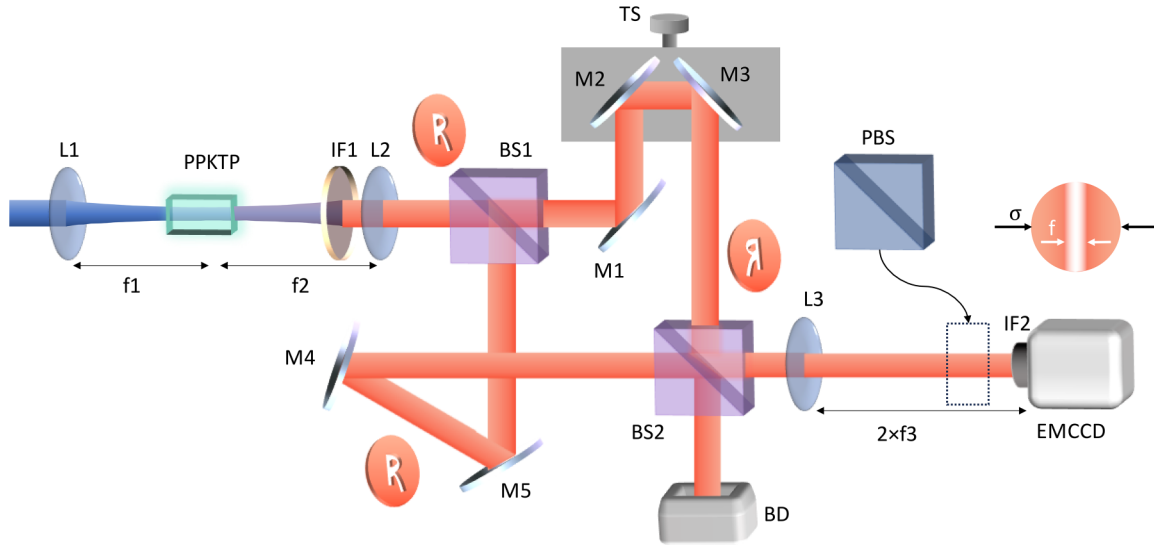


FIG. 3. Experimental setup for the measurement of Schmidt number using an odd-even Mach-Zehnder interferometer (OEMZI). Li: lens with focal length  $f_i$ , PPKTP: periodically poled potassium titanyl phosphate, TS: translation stage, IF: interference bandpass filter around 810 nm, BS: beamsplitter, EMCCD: electron multiplying charge coupled device, and BD: beam dump, M: mirror. The red circle with “R” in it indicates the flipping of the beam which happens an odd (even) number of times in the lower (upper) path. The translation stage enables movement between the minima and the maxima settings of the OEMZI.

corresponds to a vertical slice in Fig. 2, while the latter implies a horizontal slice. This can be implemented experimentally by passing the SPDC light through a narrow bandwidth filter or a small-radius aperture, respectively. Appendix C provides further comments on the properties of this wave function.

### III. EXPERIMENT AND RESULTS

#### A. Experimental setup

The goal of the experiment is to measure both  $f$  and  $\sigma$  in an interferometric method that is quick, reliable and robust. At the heart of the setup (Fig. 3) is a Mach-Zehnder interferometer that is modified to have an even number of reflections on one arm and an odd number in the other arm. We call this the odd-even Mach-Zehnder interferometer, or OEMZI. The lower arm of OEMZI has a total of three reflections at the output of BS2 (namely, from BS1, M4, and M5), while the upper arm has four reflections (from M1, M2, M3, and BS2). The mismatch in the parity of reflections ensures that the output of the OEMZI corresponds to the interference of the wave with its inversion in the  $x$  axis. This provides a direct measurement of  $W(\mathbf{q}_1, -\mathbf{q}_1)$  required in Eq. (12).

As seen in Fig. 3, a horizontally polarized Gaussian pump beam ( $\lambda_p = 405$  nm) is made incident on a periodically poled potassium titanyl phosphate (PPKTP) crystal (thickness 5 mm). The beam waist  $1/\sigma_k$  is set by lens L1. We use different lenses L1 with varying focal lengths to achieve various  $\sigma_k$ . Two different crystals (type-0 and type-2) were used to produce the two-photon SPDC states under collinear phase matching in separate experiments. The interference filter (IF) blocks the residual pump. The lens L2 (focal length 5 cm) maps the Fourier plane of the crystal center in its back focal plane. This plane is then imaged by the lens L3 (focal length 15cm) onto the EMCCD in a 2f-2f configuration. The beamsplitters BS and mirrors M form the OEMZI. A 3 mm

bandpass filter IF2 centered at 810 nm blocks all unwanted light from entering the EMCCD and ensures that only the collinear downconverted photons make it through. For the phase difference  $\delta$  between the two arms of the OEMZI, the output intensity  $I_{\text{out}}^\delta(k_x, k_y)$ , as measured by the EMCCD, is given by [48]

$$I_{\text{out}}^\delta(k_x, k_y) = \eta_e I(k_x, k_y) + \eta_o I(-k_x, k_y) + 2\sqrt{\eta_e \eta_o} W(k_x, k_y, -k_x, k_y) \cos \delta.$$

Here  $\eta_e I(k_x, k_y)$  and  $\eta_o I(k_x, k_y)$  denote the intensities observed at the EMCCD plane from the two arms of the OEMZI. The two  $\eta$ s are the scaling factors of the two arms governed by reflectivity of each surface in the respective paths.

We record our OEMZI output at the minima ( $\delta = \pi$ ) and maxima ( $\delta = 0$ ) by moving the piezo-controlled translational stage TS with a step size of about 25 nm. We repeat the above procedure for various beam waists at the crystal center by changing the focal length  $f_1$  of lens  $L_1$ .

Further, we measure the beam waist of our pump for the different  $f_1$ s by imaging the propagating beam at various distances. The widths  $w(z)$  (defined as the radius at which the intensity falls by  $1/e^2$ ) at each location  $z$  is extracted from a 2D Gaussian fit of the corresponding image. The waist  $w_0$  is then evaluated by fitting these widths  $w(z)$  of the pump with the formula for a propagating Gaussian given by [55]

$$w(z) = w_0 \sqrt{1 + \left( \frac{z \lambda_p}{\pi w_0^2 n} \right)^2}, \quad (17)$$

where  $\lambda_p$  is the pump wavelength and  $n$  is the refractive index of the medium (air in our case). More details on this measurement are presented in Appendix D.

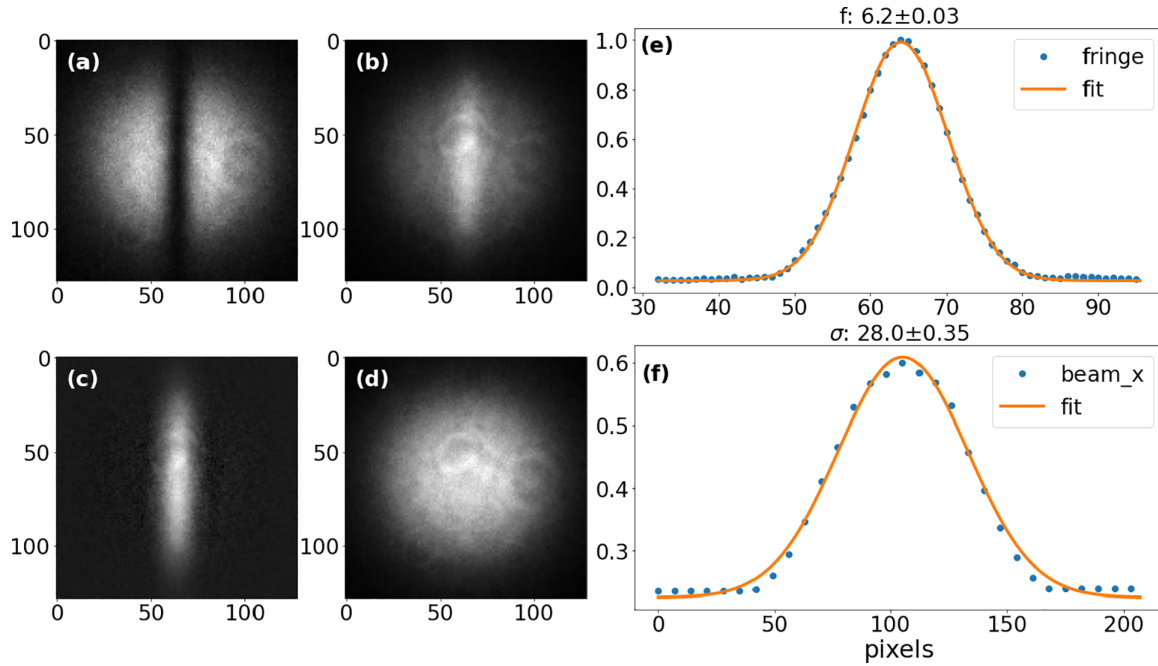


FIG. 4. Image formed on the EMCCD with 3 nm bandwidth filter as IF2 when the OEMZI is set to record (a) the minima ( $\delta = \pi$ ) and (b) the maxima ( $\delta = 0$ ). (c) The difference between (a) and (b). (d) The sum of (a) and (b). (e) The measured distribution  $P(k_{1x}|k_{2x} = 0)$  by averaging (c) along  $y$  axis (blue dots) and its fit (orange curve). (f) The measured  $P(k_x)$  by averaging (d) along  $y$  axis (blue dots) and its fit (orange curve). Here the estimated Schmidt number is  $21.1 \pm 0.6$  and L1 has a focal length of 15 cm. The fitting error for the widths is unreported as it is significantly less than the pixel width.

## B. Results and discussions

Figure 4 shows the output of our OEMZI at the two extreme settings, the maxima at  $\delta = \pi$  and the minima at  $\delta = 0$ . The difference between the two provides us the fringe  $W(k_x, k_y, -k_x, k_y)$ , while the sum of the two outputs retrieves the downconverted beam. In order to obtain the one-dimensional version of  $W(k_x, k_y, -k_x, k_y)$ , we average over the  $k_y$  values and obtain the marginal  $W(k_x, -k_x)$ , whose width yields the fringe width  $f$ . The 1D marginal probability distribution is similarly obtained from the averaging of the sum of the two settings of OEMZI, whose width is  $\sigma$ . The Schmidt number  $K$  is then calculated using Eq. (13). This is the central result of this work. Since this technique allows the measurement of  $K$  in a matter of few seconds from two images, it alleviates several issues that affect longer methods. For instance, practical factors such as the long-term stability of the laser power and its spectrum, the long-term temperature stability of the crystal are not stringent requirements for our method as they are for coincidence methods.

To test the validity of our method, we compare between the Schmidt numbers calculated from Eqs. (7) and (13). In Eq. (7),  $K$  is related to two factors, the pump beam waist  $w_0$  and the parameter  $b$ . We note that this parameter  $b$  depends only on the crystal properties (length  $L$  and refractive index  $n_c$ ) and the pump wavelength and hence remains constant throughout our experiment. The relation is given by

$$b = \sqrt{\frac{L\lambda_p}{6\pi n_c}}. \quad (18)$$

The measured beam propagation  $w(z)$  is shown in Fig. 5. The propagation follows Eq. (17) which is fit to the beam widths to obtain  $w_0$  and its location. Using these data, we not only have the waist size but also have an estimate on where to place the lens to obtain the beam waist at the crystal center.

By having experimentally measured  $K$  and  $w_0$ , we can fit a  $K$  versus  $w_0$  graph using Eq. (7) (as seen in Fig. 6) to obtain an experimental estimate of  $b$ . We see that the estimated value of  $b$  is within about 5% of the theoretically calculated  $b$  value

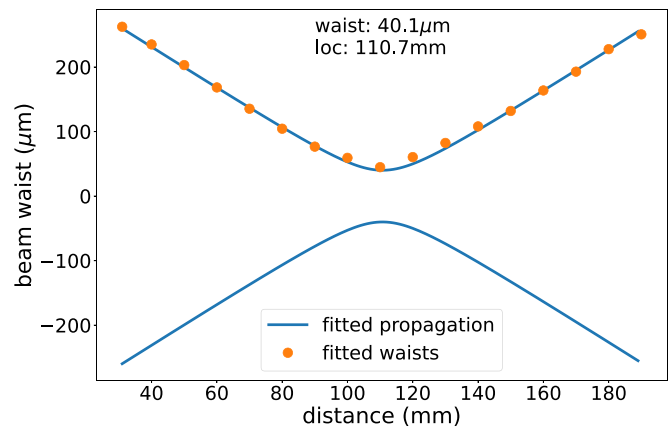


FIG. 5. The estimated pump sizes ( $w$ , orange dots) as the beam propagates are calculated by fitting 2D Gaussians on images taken of the pump as at various locations (see Appendix D). The  $w$  of the 2D fit as a function of distance is fitted to Eq. (17) (blue line) to estimate the minimum beam waist  $w_0$  and its precise location.

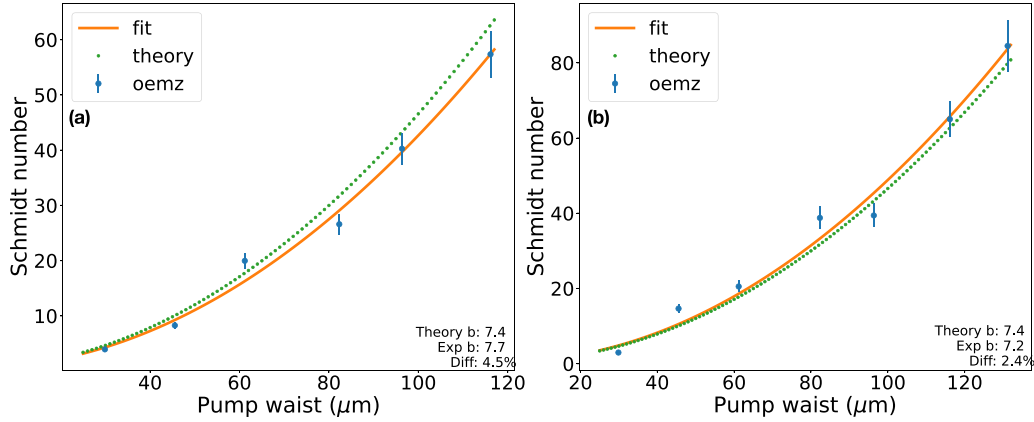


FIG. 6. Experimentally evaluated Schmidt numbers (blue dots) as calculated from Eq. (13). The orange curve shows the fit by a function given by Eq. (7) with  $b$  as the fit parameter. The theoretical curve (green dashed) given by Eq. (7) with  $b$  calculated for our experimental parameters for (a) type-0 and (b) type-2 PPKTP using Eq. (18). The fit covariance  $\Delta b = 0.002$ .

for the type-0 crystal and within 2.4% in case of type-2. The error in the final two points is higher than the rest as  $f$  was approaching the resolution limit of our camera (16 microns). This can easily be avoided by magnifying the image. This establishes that we have developed a new, quick and reliable technique to measure the Schmidt number regardless of the type of the downconverting crystal.

#### IV. CONCLUSION

In conclusion, we have demonstrated a method to rapidly measure a wide range of two-photon spatial Schmidt number at any location. Our method is based on intensity measurements, providing two orders of magnitude speedup compared to coincidence detection. Our technique works for pure two-photon states generated by SPDC, regardless of its separability as long as the condition of Eq. (11) holds. We have experimentally demonstrated its functioning for Schmidt numbers from 3 to 85 for a pure two-photon state produced by collinear phase-matching SPDC and have gotten excellent agreements with the theoretical estimates. Therefore we expect our work to have implications for a wide range of experiments and technology set to take advantage of continuous variables for quantum information applications. Furthermore, we have derived a phase-matching condition for type-2 crystals which shows the nonapplicability of the current theory to estimate the Schmidt number. We anticipate a correction to the way the beam width of SPDC is calculated will fix the discrepancy.

#### ACKNOWLEDGMENTS

We thank Sreeman Kumar for his instrumental role in setting up the instrumentation for an early version of our experiment. We also express our gratitude to the Department of Atomic Energy, Government of India, for funding for Project Identification No. RTI4002 under DAE OM No. 1303/1/2020/R&D-II/DAE/5567. The authors declare no conflict of interest.

V.S.B. and K.B. have contributed equally to this work.

#### APPENDIX A: RELATION BETWEEN THE RATIO OF WIDTHS AND THE VISIBILITY OF INTERFERENCE

It was pointed out in Ref. [42] that the Schmidt number is inversely proportional to the output of their inversion interferometer as

$$K = \frac{P_+ + P_-}{P_+ - P_-}, \quad (\text{A1})$$

where  $P_{\pm}$  is the (conditional) count rate at the constructive/destructive port of the interferometer. In the context of OEMZI, this corresponds to the inverse total visibility of the interference.

The marginal distribution of Fig. 4 is given by a Gaussian with a width  $\sigma$  while the fringe is given by a Gaussian with a width  $f$ . Thus the (y-averaged) output of OEMZI at minima is the difference of the two Gaussians and their sum is the maxima. Using the fact that the area of a Gaussian of width  $\sigma$  is given by  $\sqrt{\pi}\sigma$ , the total intensity at the minima is  $\sqrt{\pi}\sigma - \sqrt{\pi}f$  and the total intensity at the maxima is  $\sqrt{\pi}\sigma + \sqrt{\pi}f$  thus the inverse visibility is given by

$$\frac{1}{V} = \frac{(\sqrt{\pi}\sigma + \sqrt{\pi}f) + (\sqrt{\pi}\sigma - \sqrt{\pi}f)}{(\sqrt{\pi}\sigma + \sqrt{\pi}f) - (\sqrt{\pi}\sigma - \sqrt{\pi}f)} = \frac{\sigma}{f}. \quad (\text{A2})$$

Once more, invoking azimuthal symmetry we finally get the 2D Schmidt number as the square of the inverse visibility to get an expression equivalent to Eq. (13):

$$K = \frac{1}{V^2} = \left(\frac{\sigma}{f}\right)^2. \quad (\text{A3})$$

Since the ratio of the widths of the beam and the fringe is just the inverse visibility, it implies that at any plane in the propagation gives us the Schmidt number which can be seen in Fig. 7.

#### APPENDIX B: TYPE-2 WITH 10 nm FILTER

Here, we discuss the consequences of the nondegenerate light contaminating the measurement. We performed a set of experiments with a type-2 crystal using a 10 nm bandwidth filter. Figure 8, arranged similar to Fig. 4, elucidates

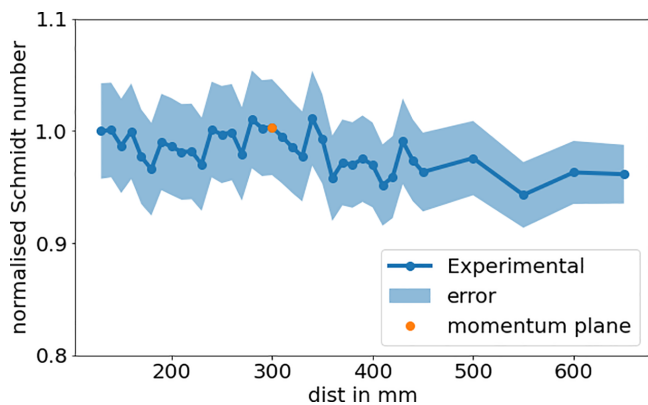


FIG. 7. The normalized Schmidt number measured (blue curve) by OEMZI at various locations along the propagation. The momentum plane (orange point) is where we conducted the main experiment. The flatness indicates that OEMZI measures the Schmidt number at any location.

the results. We observed that the downconverted beam shape shown in Fig. 8(f) approximated a top-hat function rather than a Gaussian. This renders the DG approximation invalid. Furthermore, the apparent width of the beam turns out to be about double of the theoretical estimate given by  $b$ , which was accurately reproduced in the narrowband experiments of Fig. 4. This discrepancy led to the overestimation of the Schmidt number as compared to the theoretical predictions.

Our experimental estimate for the  $b$  parameter was off by a substantial amount, precisely, 61%. Since the theory predicted a much smaller beam diameter, the source of this discrepancy

was in the beam size. While deriving the wave function, we had made the assumption that the SPDC photons were degenerate. Upon recalculation (shown in Sec. II B) without the degeneracy condition, the phase-matching conditions gave rise to a  $\text{sinc}^2(A + Bq_-^2)$  rather than the expected  $\text{sinc}^2(q_-^2)$ . The extra  $A$  (collinear phase mismatch) causes noncollinear contributions leading to a larger beam size.

The maximas of the wave function of the form  $\text{sinc}^2$  with Eq. (16) as its argument, obey the following transcendental equation:

$$\tan(\Delta k_z) = \Delta k_z. \quad (\text{B1})$$

The above equation leads to two equal maxima for the wave function whenever the argument of the tan function is negative at  $q_- = 0$ . This implies that whenever the following inequality holds:

$$\frac{n_p}{\lambda_p} - \frac{1}{\Lambda} < \frac{n_1}{\lambda_1} + \frac{n_2}{\lambda_2} \Rightarrow \frac{n_p - n_2}{\lambda_p} - \frac{1}{\Lambda} < \frac{n_1 - n_2}{\lambda_1}, \quad (\text{B2})$$

we get a ring-like emission for those wavelength pairs, as shown in Fig. 10. For all the wavelength pairs where the inequality is violated, we get an approximate Gaussian-like emission. In the above inequality, we have made use of energy conservation to rewrite  $\lambda_2$  in terms of  $\lambda_p$  and  $\lambda_1$ . The final EMCCD image is an accumulation of all such wavelength pairs that build up to the top-hat beam seen in Fig. 8.

To test our hypothesis on type-2 conversion, we used a sharper 3 nm bandwidth filter, thereby restricting the possible wavelength pairs reaching the EMCCD to those that do not violate the Ineq. (B2). This allows the wave function be well approximated by a double-Gaussian. The experiment with

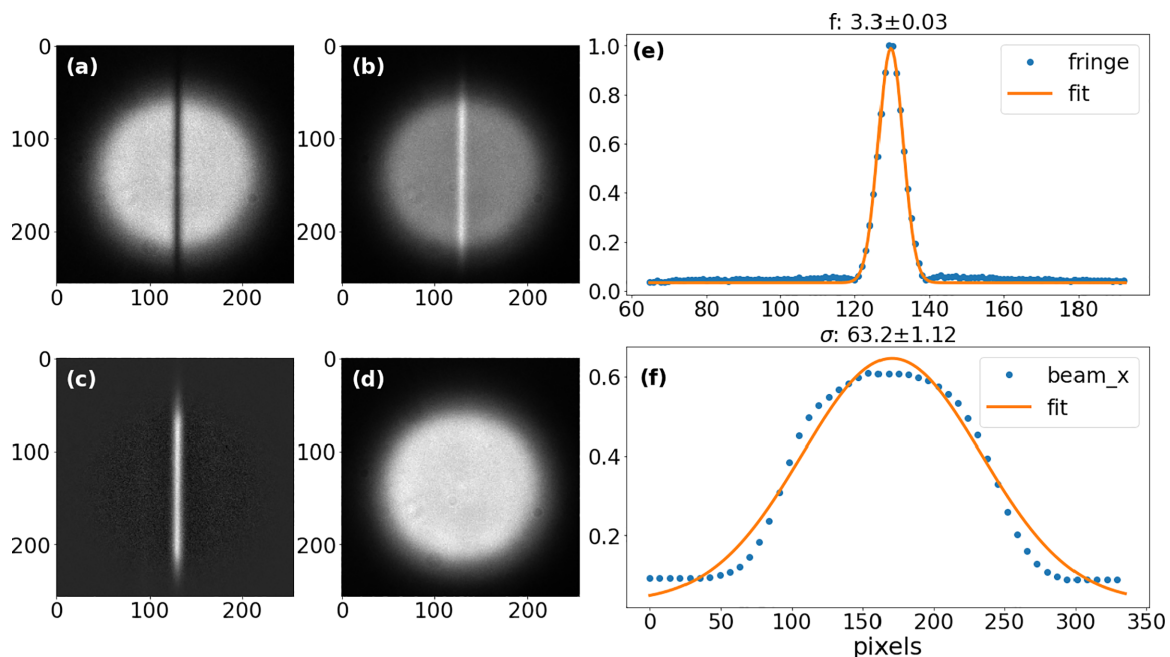


FIG. 8. Image formed on the EMCCD with 10 nm bandwidth filter as IF2 when the OEMZI is set to record (a) the minima ( $\delta = \pi$ ) and (b) the maxima ( $\delta = 0$ ). (c) The difference between (a) and (b). (d) The sum of (a) and (b). (e) The measured  $P(q_1|q_2 = 0)$  by averaging (c) along  $y$  axis (blue dots) and its fit (orange curve). (f) The measured  $P(q_1)$  by averaging (d) along  $y$  axis (blue dots) and its fit (orange curve). Noncollinear contributions from the nondegenerate SPDC results in severe deviations from the Gaussian fit. Here L1 has a focal length of 30 cm.

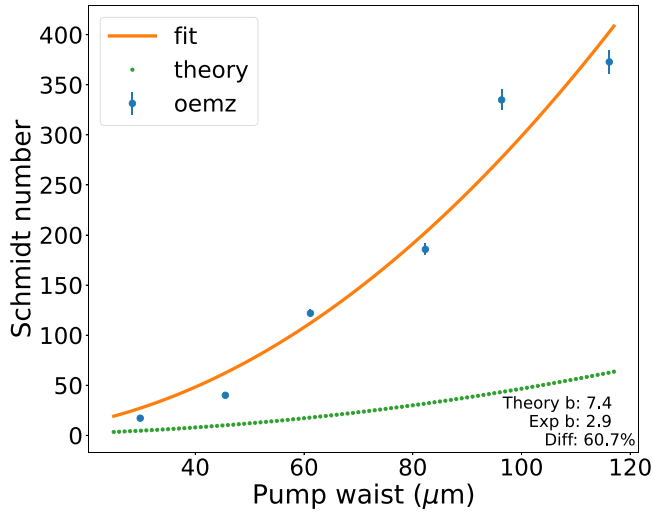


FIG. 9. Experimentally evaluated Schmidt numbers (blue dots) as calculated from Eq. (13) using a 10 nm bandwidth filter. The orange curve shows the fit by the function given by Eq. (7) with  $b$  as the fit parameter. The theoretical curve (green dashed) given by Eq. (7) with  $b$  calculated for our experimental parameters for type-2 PPKTP using Eq. (18).

sharper filters revealed that the discrepancy of 61% between theory and experiment (Fig. 9) was significantly reduced to <2% as seen in Fig. 6.

Interestingly, one can see from Fig. 9 that even though the experimental curve is very off from the theoretical one, the form of Eq. (7) (the orange curve in Fig. 9) fits the data quite well. We anticipate that this discrepancy will be resolved by a better theoretical estimate of the beam size  $\sigma$ . It is interesting to see that even though the closed form of the Schmidt number in Eq. (7) was derived for the simplistic case of a DG, it still captures the essential functional form of the states created and

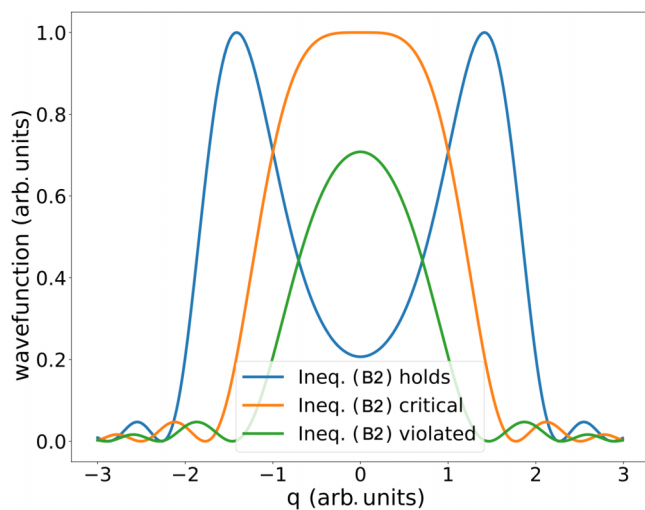


FIG. 10. Type-2 crystal for certain wavelength pairs. The blue curve is when the daughter photons have excess momentum [Ineq. (B2) holds] showing the ring structure. The green curve is when Ineq. (B2) is violated which shows an approximate Gaussian structure. The orange curve shows the critical stage where Ineq. (B2) becomes an equality.

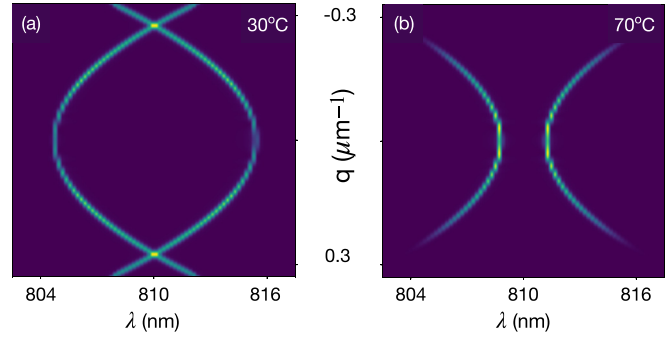


FIG. 11. Type-2 wave function generated at a temperature of (a) 30 °C and (b) 70 °C. The separation between the signal and idler curves increase with increasing temperature. The granularity is an artefact of the low sampling rate

measured in laboratories. This likely originates from the inherent azimuthal symmetry of beams that leads to a quadratic relation.

### APPENDIX C: MEASUREMENT OF THE SPATIOSPECTRAL PROPERTIES OF THE WAVE FUNCTION

Since our experimental beam width for type-2 crystal in the momentum space was much wider than the theoretical estimate, we wanted to experimentally study its spatio-spectral properties. We measure the spatio-spectrogram of the SPDC (Fig. 2) using a slit and a grating. This corresponds to projecting the wave function from Sec. II B in the transverse momentum and wavelength basis.

To see the Ineq. (B2) manifest itself in the spatio-spectrum, consider two wavelength slices in Fig. 2. One near the degenerate center of 810 nm and another at the off-centre 805/815 nm. For the off-centre slice, the wave function has finite contributions only from two small diametrically opposite regions around  $q = \pm 0.3 \mu\text{m}^{-1}$ . This is when the Ineq. (B2) is violated and corresponds to the blue curve with two peaks in Fig. 10. This ringlike structure gets smaller and smaller the closer our slice gets to the central wavelength. The critical condition (orange curve in Fig. 10) is achieved when the signal and idler curves just touch each other at the central wavelength.

We also studied the temperature dependence of the spatio-spectral property. We see that the focus of the two curves shifted with temperature, bring them closer/farther as can be seen in Figs. 11(a) and 11(b). We found that for temperatures greater than 40 °C (which is the optimal temperature to get the most degenerate pairs from our crystal) the two curves stop overlapping and get separated. At these temperatures, the SPDC beam looks like a ring and is deemed noncollinear. What our spatio-spectral exploration showed us is that there are significant noncollinear contributions even at the optimal temperature and that a sharp spectral filter is needed to filter out only the central degenerate collinear portion.

### APPENDIX D: BEAM WAIST MEASUREMENT

As seen from the theoretical considerations above, an accurate measurement of the beam waist is quite important as our

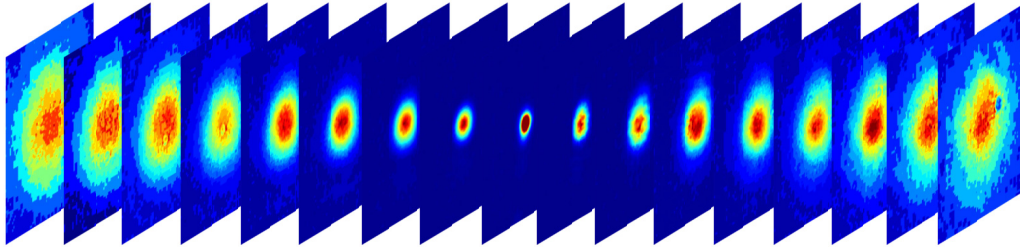


FIG. 12. Images of the pump beam taken 10 cm apart as it propagates in free space after a 10 cm focal length lens. Each image comprises  $150 \times 150$  pixels with pixel size of  $3.6 \mu\text{m}$ .

theoretical estimate for the Schmidt number depends on it in the form given by Eq. (7). For lower values in our experiment ( $\sim 25 \mu\text{m}$ ), a direct imaging of the waist is prone to errors since our pixel size was  $3.7 \mu\text{m}$ . Alternately, one could build a magnified imaging system, which however, would require measuring three parameters accurately, the focal length of the lens, the image and object distances. Therefore we used a fitting subroutine on a multiposition measurement of the focus.

The fact that we spatially filter our pump means that the pump follows a Gaussian beam propagation and thus the waist  $w$  at any location is given by Eq. (17) which is a

two-parameter function. Thus, we can image our pump beam at various locations as it propagates (see Fig. 12) and use Eq. (17) to fit it for a better estimate of not just the beam waist but also the waist location.

Accordingly, a 2D Gaussian is first fit to each image and its standard deviation along the horizontal axis (since our OEMZI flips only this axis) is taken as the estimate of the beam waist  $w$  at that location  $z$ . The curve of these estimated waists as a function of the propagation distance is shown in Fig. 5 which is fit by the function given by Eq. (17). The minimum represented by this curve is given by the fitting parameter.

- 
- [1] A. Einstein, B. Podolsky, and N. Rosen, Can quantum-mechanical description of physical reality be considered complete? *Phys. Rev.* **47**, 777 (1935).
- [2] E. Schrödinger, Die gegenwärtige situation in der quantenmechanik, *Naturwissenschaften* **23**, 807 (1935).
- [3] D. Bohm, *Quantum Theory* (Englewood Cliffs, NJ, Prentice-Hall, 1951)
- [4] J. S. Bell, On the Einstein Podolsky Rosen paradox, *Phys. Phys. Fiz.* **1**, 195 (1964).
- [5] S. J. Freedman and J. F. Clauser, Experimental test of local hidden-variable theories, *Phys. Rev. Lett.* **28**, 938 (1972).
- [6] A. Aspect, P. Grangier, and G. Roger, Experimental tests of realistic local theories via Bell's theorem, *Phys. Rev. Lett.* **47**, 460 (1981).
- [7] A. Aspect, P. Grangier, and G. Roger, Experimental realization of Einstein-Podolsky-Rosen-Bohm gedankenexperiment: A new violation of Bell's inequalities, *Phys. Rev. Lett.* **49**, 91 (1982).
- [8] A. Aspect, J. Dalibard, and G. Roger, Experimental test of bell's inequalities using time-varying analyzers, *Phys. Rev. Lett.* **49**, 1804 (1982).
- [9] R. F. Werner, Quantum states with Einstein-Podolsky-Rosen correlations admitting a hidden-variable model, *Phys. Rev. A* **40**, 4277 (1989).
- [10] D. Cozzolino, B. Da Lio, D. Bacco, and L. K. Oxenløwe, High-dimensional quantum communication: Benefits, progress, and future challenges, *Adv. Quantum Technol.* **2**, 1900038 (2019).
- [11] M. Erhard, M. Malik, and A. Zeilinger, A quantum router for high-dimensional entanglement, *Quantum Sci. Technol.* **2**, 014001 (2017).
- [12] F.-G. Deng, B.-C. Ren, and X.-H. Li, Quantum hyperentanglement and its applications in quantum information processing, *Sci. Bull.* **62**, 46 (2017).
- [13] S. Ecker, F. Bouchard, L. Bulla, F. Brandt, O. Kohout, F. Steinlechner, R. Fickler, M. Malik, Y. Guryanova, R. Ursin, and M. Huber, Overcoming noise in entanglement distribution, *Phys. Rev. X* **9**, 041042 (2019).
- [14] N. Gisin and S. Massar, Optimal quantum cloning machines, *Phys. Rev. Lett.* **79**, 2153 (1997).
- [15] F. Bouchard, R. Fickler, R. W. Boyd, and E. Karimi, High-dimensional quantum cloning and applications to quantum hacking, *Sci. Adv.* **3**, e1601915 (2017).
- [16] J. T. Barreiro, T.-C. Wei, and P. G. Kwiat, Beating the channel capacity limit for linear photonic superdense coding, *Nat. Phys.* **4**, 282 (2008).
- [17] G. Adesso and F. Illuminati, Entanglement in continuous-variable systems: recent advances and current perspectives, *J. Phys. A: Math. Theor.* **40**, 7821 (2007).
- [18] M. L. Almeida, S. Pironio, J. Barrett, G. Tóth, and A. Acín, Noise robustness of the nonlocality of entangled quantum states, *Phys. Rev. Lett.* **99**, 040403 (2007).
- [19] F. Zhu, M. Tyler, N. H. Valencia, M. Malik, and J. Leach, Is high-dimensional photonic entanglement robust to noise? *AVS Quantum Sci.* **3**, 011401 (2021).
- [20] N. Friis, G. Vitagliano, M. Malik, and M. Huber, Entanglement certification from theory to experiment, *Nat. Rev. Phys.* **1**, 72 (2018).
- [21] M. D'Angelo, Y.-H. Kim, S. P. Kulik, and Y. Shih, Identifying entanglement using quantum ghost interference and imaging, *Phys. Rev. Lett.* **92**, 233601 (2004).

- [22] J. C. Howell, R. S. Bennink, S. J. Bentley, and R. W. Boyd, Realization of the Einstein-Podolsky-Rosen paradox using momentum- and position-entangled photons from spontaneous parametric down conversion, *Phys. Rev. Lett.* **92**, 210403 (2004).
- [23] W. Zhang, R. Fickler, E. Giese, L. Chen, and R. W. Boyd, Influence of pump coherence on the generation of position-momentum entanglement in optical parametric down-conversion, *Opt. Express* **27**, 20745 (2019).
- [24] M. N. O’Sullivan-Hale, I. A. Khan, R. W. Boyd, and J. C. Howell, Pixel entanglement: Experimental realization of optically entangled  $d = 3$  and  $d = 6$  qudits, *Phys. Rev. Lett.* **94**, 220501 (2005).
- [25] J. Leach, R. E. Warburton, D. G. Ireland, F. Izdebski, S. M. Barnett, A. M. Yao, G. S. Buller, and M. J. Padgett, Quantum correlations in position, momentum, and intermediate bases for a full optical field of view, *Phys. Rev. A* **85**, 013827 (2012).
- [26] M. Edgar, D. Tasca, F. Izdebski, R. Warburton, J. Leach, M. Agnew, G. Buller, R. Boyd, and M. Padgett, Imaging high-dimensional spatial entanglement with a camera, *Nat. Commun.* **3**, 984 (2012).
- [27] M. Reichert, H. Defienne, and J. W. Fleischer, Massively parallel coincidence counting of high-dimensional entangled states, *Sci. Rep.* **8**, 7925 (2018).
- [28] P.-A. Moreau, F. Devaux, and E. Lantz, Einstein-podolsky-rosen paradox in twin images, *Phys. Rev. Lett.* **113**, 160401 (2014).
- [29] J. Leach, B. Jack, J. Romero, A. K. Jha, A. M. Yao, S. Franke-Arnold, D. G. Ireland, R. W. Boyd, S. M. Barnett, and M. J. Padgett, Quantum correlations in optical angle-orbital angular momentum variables, *Science* **329**, 662 (2010).
- [30] L. Chen, T. Ma, X. Qiu, D. Zhang, W. Zhang, and R. W. Boyd, Realization of the Einstein-Podolsky-Rosen paradox using radial position and radial momentum variables, *Phys. Rev. Lett.* **123**, 060403 (2019).
- [31] Z. Y. Ou, S. F. Pereira, H. J. Kimble, and K. C. Peng, Realization of the Einstein-Podolsky-Rosen paradox for continuous variables, *Phys. Rev. Lett.* **68**, 3663 (1992).
- [32] I. A. Khan and J. C. Howell, Experimental demonstration of high two-photon time-energy entanglement, *Phys. Rev. A* **73**, 031801(R) (2006).
- [33] J.-P. W. MacLean, J. M. Donohue, and K. J. Resch, Direct characterization of ultrafast energy-time entangled photon pairs, *Phys. Rev. Lett.* **120**, 053601 (2018).
- [34] Y. Mei, Y. Zhou, S. Zhang, J. Li, K. Liao, H. Yan, S.-L. Zhu, and S. Du, Einstein-Podolsky-Rosen energy-time entanglement of narrow-band biphotons, *Phys. Rev. Lett.* **124**, 010509 (2020).
- [35] M. Agnew, J. Leach, M. McLaren, F. S. Roux, and R. W. Boyd, Tomography of the quantum state of photons entangled in high dimensions, *Phys. Rev. A* **84**, 062101 (2011).
- [36] D. Giovannini, J. Romero, J. Leach, A. Dudley, A. Forbes, and M. J. Padgett, Characterization of high-dimensional entangled systems via mutually unbiased measurements, *Phys. Rev. Lett.* **110**, 143601 (2013).
- [37] J. Bavaresco, N. Herrera Valencia, C. Klöckl, M. Pivoluska, P. Erker, N. Friis, M. Malik, and M. Huber, Measurements in two bases are sufficient for certifying high-dimensional entanglement, *Nat. Phys.* **14**, 1032 (2018).
- [38] Z. Hou, J.-F. Tang, C. Ferrie, G.-Y. Xiang, C.-F. Li, and G.-C. Guo, Experimental realization of self-guided quantum process tomography, *Phys. Rev. A* **101**, 022317 (2020).
- [39] M. Rambach, M. Qaryan, M. Kewming, C. Ferrie, A. G. White, and J. Romero, Robust and efficient high-dimensional quantum state tomography, *Phys. Rev. Lett.* **126**, 100402 (2021).
- [40] I. Nape, V. Rodríguez-Fajardo, F. Zhu, H.-C. Huang, J. Leach, and A. Forbes, Measuring dimensionality and purity of high-dimensional entangled states, *Nat. Commun.* **12**, 5159 (2021).
- [41] K. W. Chan, J. P. Torres, and J. H. Eberly, Transverse entanglement migration in Hilbert space, *Phys. Rev. A* **75**, 050101(R) (2007).
- [42] F. Just, A. Cavanna, M. V. Chekhova, and G. Leuchs, Transverse entanglement of biphotons, *New J. Phys.* **15**, 083015 (2013).
- [43] B. Courme, C. Vernière, P. Svihra, S. Gigan, A. Nomerotski, and H. Defienne, Quantifying high-dimensional spatial entanglement with a single-photon-sensitive time-stamping camera, *Opt. Lett.* **48**, 3439 (2023).
- [44] J. Ma, S. Masoodian, D. A. Starkey, and E. R. Fossum, Photon-number-resolving megapixel image sensor at room temperature without avalanche gain, *Optica* **4**, 1474 (2017).
- [45] R. Chatterjee, V. S. Bhat, K. Bajar, and S. Mujumdar, Multi-fold enhancement of quantum SNR by using an EMCCD as a photon number resolving device, *Optica Quantum* **2**, 156 (2024).
- [46] B. M. Terhal and P. Horodecki, Schmidt number for density matrices, *Phys. Rev. A* **61**, 040301(R) (2000).
- [47] H. Di Lorenzo Pires, C. H. Monken, and M. P. van Exter, Direct measurement of transverse-mode entanglement in two-photon states, *Phys. Rev. A* **80**, 022307 (2009).
- [48] G. Kulkarni, R. Sahu, O. S. Magaña-Loaiza, R. W. Boyd, and A. K. Jha, Single-shot measurement of the orbital-angular-momentum spectrum of light, *Nat. Commun.* **8**, 1054 (2017).
- [49] A. Bhattacharjee, N. Meher, and A. K. Jha, Measurement of two-photon position-momentum Einstein-Podolsky-Rosen correlations through single-photon intensity measurements, *New J. Phys.* **24**, 053033 (2022).
- [50] C. K. Law and J. H. Eberly, Analysis and interpretation of high transverse entanglement in optical parametric down conversion, *Phys. Rev. Lett.* **92**, 127903 (2004).
- [51] J. Schneeloch and J. C. Howell, Introduction to the transverse spatial correlations in spontaneous parametric down-conversion through the biphoton birth zone, *J. Opt.* **18**, 053501 (2016).
- [52] M. V. Fedorov, Y. M. Mikhailova, and P. A. Volkov, Gaussian modelling and schmidt modes of spdc biphoton states, *J. Phys. B: At., Mol. Opt. Phys.* **42**, 175503 (2009).
- [53] K. Kato and E. Takaoka, Sellmeier and thermo-optic dispersion formulas for ktp, *Appl. Opt.* **41**, 5040 (2002).
- [54] F. M. Miatto, H. Di Lorenzo Pires, S. M. Barnett, and M. P. van Exter, Spatial schmidt modes generated in parametric down-conversion, *Eur. Phys. J. D* **66**, 263 (2012).
- [55] O. Svelto, Ray and wave propagation through optical media, in *Principles of Lasers* (Springer, US, 2009), pp. 131–161.